Gem News International

Contributing Editors
Emmanuel Fritsch, *University of Nantes, CNRS, Team 6502, Institut des Matériaux Jean Rouxel (IMN), Nantes, France* (fritsch@cnrs-imn.fr)
Gagan Choudhary, *Gem Testing Laboratory, Jaipur, India* (gagan@gjepcindia.com)
Christopher M. Breeding, *GIA, Carlsbad* (christopher.breeding@gia.edu)

COLORED STONES AND ORGANIC MATERIALS

New emerald locality in Southern California. Located about 60 miles east of San Diego, a new emerald deposit has been discovered in the Julian Mining District (figure 1). This area is known for pegmatite mines and hydrothermal mineral deposits; however, none of those are known to have produced emeralds to date. The emeralds (example shown in figure 2) were all collected by author RE and son Bruce Edley near the surface and are embedded in a biotite schist host rock. Most of the recovered single crystals have a translucent dark green color and inclusions, and they are typically smaller than 2 cm. A few light-colored green beryl crystals have been recovered from a nearby pegmatite. Their formation was likely correlated with metamorphic and hydrothermal processes associated with regional tectonism.

Figure 1. A map of California with an inset showing the San Diego area and marking the emerald locality (star).

Figure 2. An example of an emerald cluster found in a new deposit in Julian, California. Specimen size is 20 × 10 × 9 mm. Photo by Myke Clarkson.

Samples were analyzed at the Natural History Museum of Los Angeles County and sent to GIA for species confirmation using laser ablation–inductively coupled plasma–mass spectroscopy (LA-ICP-MS). We performed Raman and X-ray fluorescence (XRF) hyperspectral mapping and powder X-ray diffraction (not shown) to determine mineralogy

Editors' note: Interested contributors should send information and illustrations to Stuart Overlin at soverlin@gia.edu or GIA, The Robert Mouawad Campus, 5345 Armada Drive, Carlsbad, CA 92008.

Gems & Gemology, Vol. 56, No. 4 pp. 542–554.

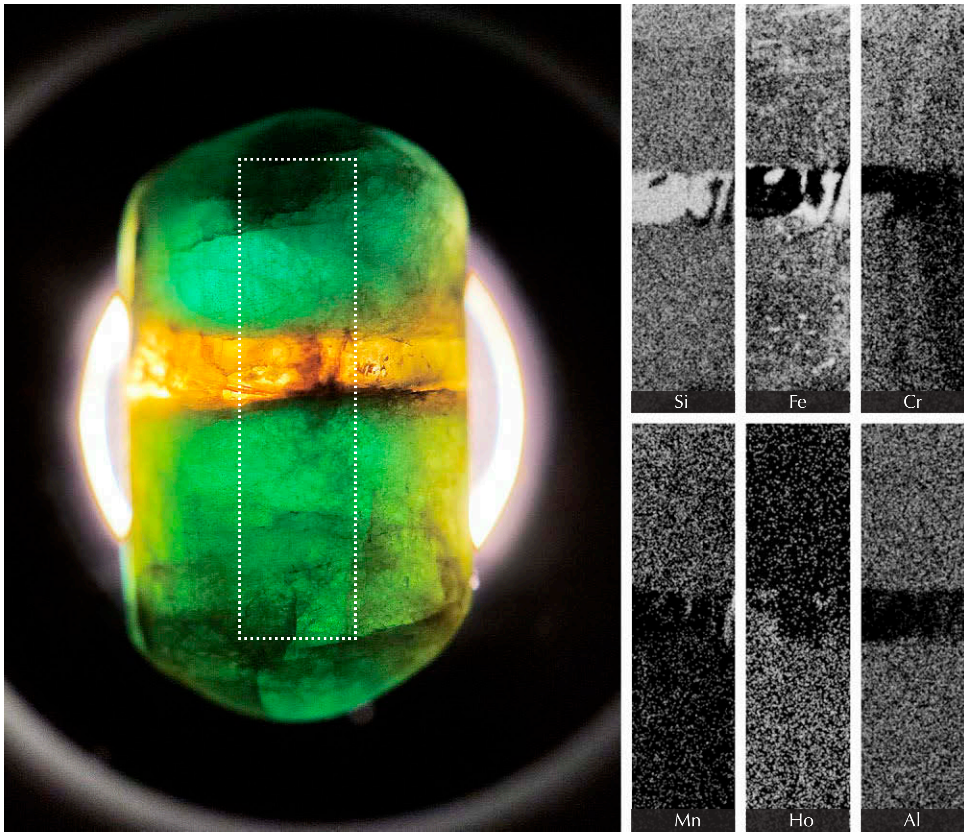

Figure 3. Left: A 3.16 ct polished pill-shaped emerald, seen in transmitted light, was one of the best examples of emerald with citrine from this locality. Photo by Aaron Celestian. Right: Element maps of the outlined area on the specimen. Brighter areas indicate higher concentrations.

and elemental composition. Raman analysis on a polished pill-shaped gem (figure 3, left) identified beryl and quartz to confirm our observation of the rare combination of emerald and citrine. Raman further identified dolomite and hematite inclusions. XRF element maps (figure 3, right) show silicon (Si), chromium (Cr), magnesium (Mg), iron (Fe), aluminum (Al), and holmium (Ho) content. Of the approximately 425 carats of emeralds that have been recovered, about 5–10% contain macro-citrine inclusions, representing a unique aspect of this deposit.

The distribution of trace elements in the pill-shaped emerald indicates a complex series of events. The emerald is cross-cut by a layer of citrine. Half of the gem is enriched in trace holmium (below the citrine), where holmium is inversely correlated with manganese. Chromium-rich areas run perpendicular to the citrine, but align on either side of the citrine, suggesting that the emerald formed as a single crystal. The patterns of holmium and manganese hint toward secondary geochemical processes that may be related to later citrine emplacement, though the origin of these processes is unknown. The unusual mineral associations and elemental distribution demonstrate the geologic complexity of the deposit, and further work is needed to unravel its full history.

Aaron J. Celestian (acelestian@nhm.org)
Natural History Museum of Los Angeles County

Richard Edley
Banning, California

Update on inclusions in emeralds from Davdar, China. We recently had the opportunity to examine emeralds containing unknown solid inclusions and numerous multiphase inclusions reportedly from Davdar, China. Three green transparent rough samples were acquired from the former mine owner Guimin Wong. They weighed 0.55 0.45, and 0.50 ct, respectively, with a diameter from 4.0 to 5.0 mm, a refractive index of 1.578 ± 0.002–1.584 ± 0.001, and SG ranging from 2.64 to 2.76. They were inert to both long- and short-wave UV radiation. Inclusion features of Davdar emeralds have been reported previously in the literature.

Very few mineral species have been identified as inclusions in this emerald—these include feldspar (plagioclase) (S. Saeseaw et al., "Three-phase inclusions in emerald and their impact on origin determination," Summer 2014 *G&G*, pp. 114–132; S. Saeseaw et al., "Geographic origin determination of emerald," Winter 2019 *G&G*, pp. 614–646) and to a lesser extent tourmaline, mica, scheelite, and fluorite (D. Marshall, "Geological work," *InColor*, Spring 2009, p. 29). Black rounded crystals were observed in some of the Davdar emeralds we studied. Previous studies noted the presence of black minerals as well but did not identify them (S. Saeseaw et al., 2014, 2019). We revealed the black mineral to be magnetite via Raman microspectrometry (figure 4). This is potentially the first time magnetite has been identified in Davdar emeralds, though it has been identified in emeralds from other regions (referenced

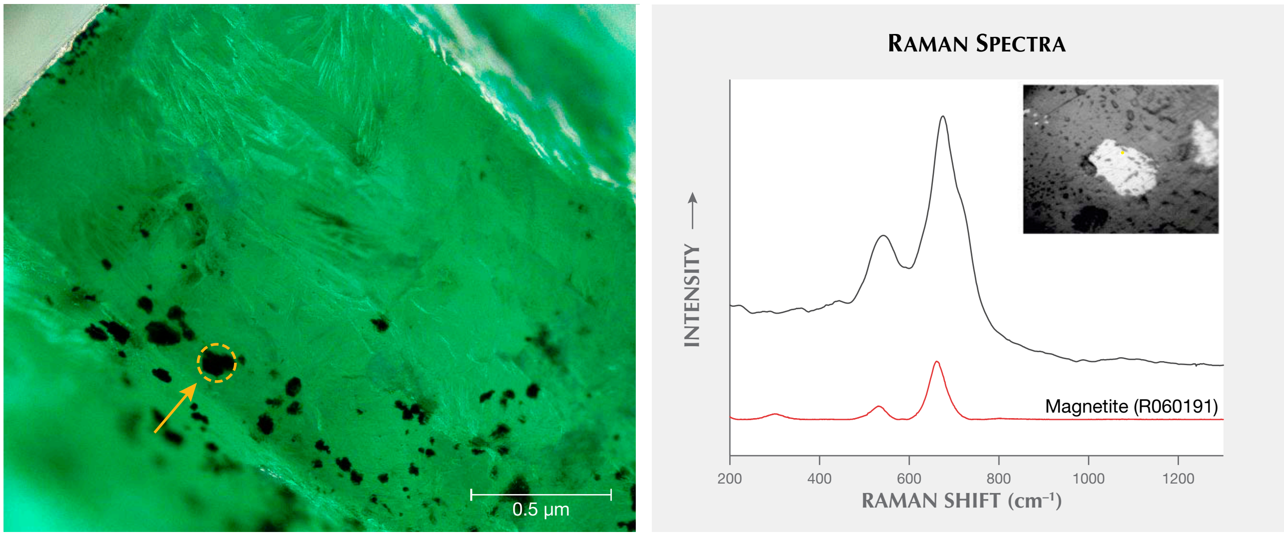

Figure 4. Left: A Davdar emerald hosted numerous black mineral inclusions identified by laser Raman microspectrometry as magnetite. Right: The Raman spectrum of the inclusions is shown along with the Raman reference spectrum for magnetite in the RRUFF database. Spectra are offset for clarity. Inset photomicrograph by Di Cui.

above). Magnetite as a black iron oxide inclusion is commonly seen in emeralds from Zambian and Brazilian localities and other schist-hosted origins (again, see Saeseaw et al., 2019).

Multiphase inclusions occur commonly in Davdar emeralds with solid phases (mainly halides such as halite assumed by D. Marshall et al., "Conditions for emerald formation at Davdar, China: Fluid inclusion, trace element and stable isotope studies," *Mineralogical Magazine*, Vol. 76, No. 1, 2012, pp. 213–226). Since previous studies reported that some birefringent phases did not dissolve during heating (again, see Marshall et al., 2012), we hoped to learn the solid phase identity in fluid inclusions. Comprehensive microscopic and Raman spectroscopic analyses indicated the presence of dolomite and likely calcite daughter inclusions (figures 5 and 6). As the solubility of a carbonate such as calcite seems to show an inverse solubility with respect to temperature (see B. Coto et al., "Effects in the

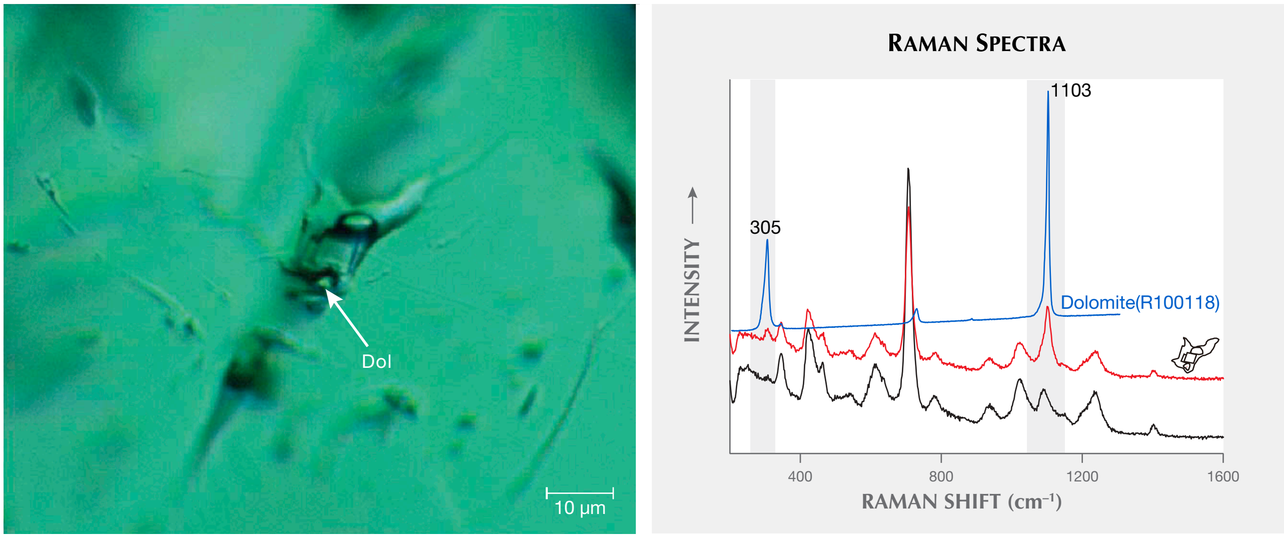

Figure 5. Left: Solid-rich fluid inclusions in Davdar emerald. One of the solid phases was determined to be dolomite. Right: The corresponding spectrum (red) showed peaks from both the host beryl (black) and the reference spectrum for dolomite in the RRUFF database (blue). Photomicrograph by Di Cui.

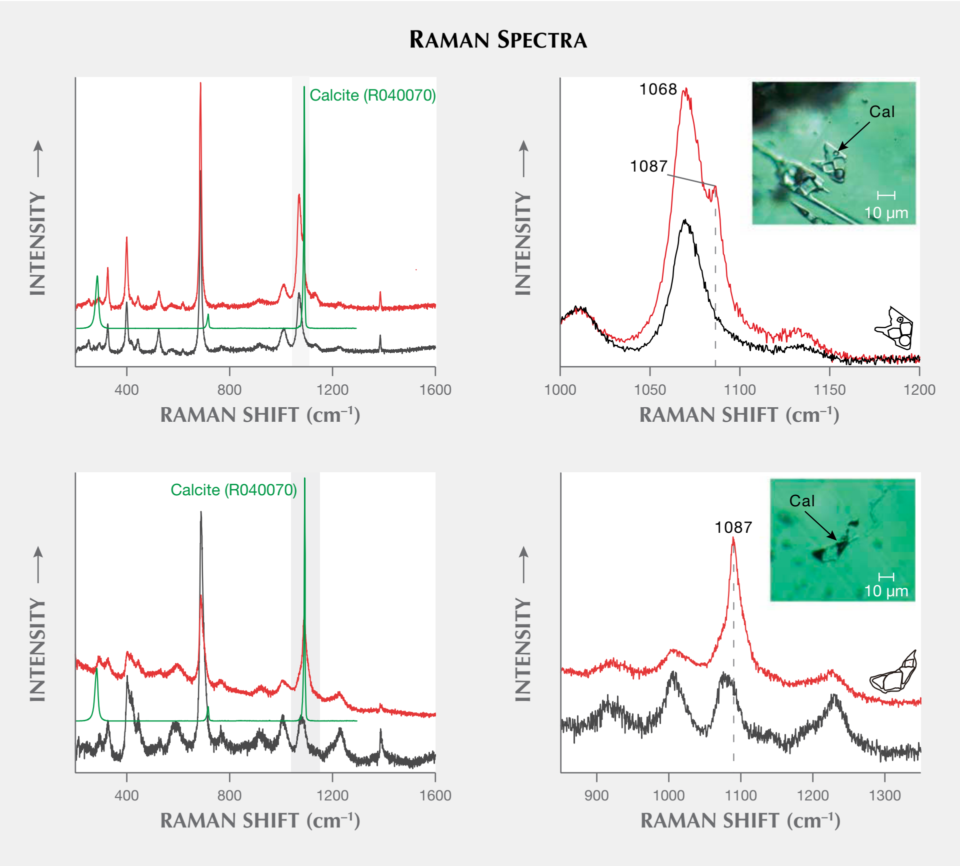

Figure 6. Two daughter crystals in separate inclusions were identified as likely calcite based on comparison with Raman reference spectra from the RRUFF database. The top and bottom left images show the spectra of the two daughter inclusions (red), the host beryl (black), and the RRUFF calcite reference spectrum (green). The dominant calcite peak at 1087 cm^{-1} matches with weak peaks in both daughter crystals. The top and bottom right images show the weak 1087 cm^{-1} peak corresponding to calcite under magnification. Photomicrographs by Di Cui.

solubility of $CaCO_3$: Experimental study and model description," *Fluid Phase Equilibria*, Vol. 324, 2012, pp. 1–7), the first identified dolomite daughter crystals could be attributable to the phases that were insoluble with increasing temperature and added more constraints to fluid inclusions in Davdar emeralds.

As far as we are aware, the carbonate phase could simply refer to the local geologic background and the host rock lithology, which mainly consisted of sandstone and dolomitic limestone. Study of the inclusions showed interesting results due to the genetic environment of the Davdar emerald mine. In addition to the daughter chloride such as halite, the identified dolomite mineral defined the complex multiphase assemblage for the Davdar fluid inclusion population.

Di Cui, Zongting Liao, Lijian Qi, and Zhengyu Zhou
School of Ocean and Earth Science
Laboratory of Gem and Technological Materials
Tongji University

Dendritic inclusions in nephrite from Dahua, China. Since the 2010s, with the discovery of nephrite ore deposits in Luodian County, Guizhou Province, a significant amount of nephrite has been mined in the town of Yantan in Dahua Yao Autonomous County, located in the northwest of the Guangxi Zhuang Autonomous Region (Z. Yin et al., "Nephrite jade from Guangxi Province, China," Fall 2014 *G&G*, pp. 228–235). Previously we reported on the nature of the chlorite inclusions found in this nephrite, and here we identify the chlorite as penninite.

The discovery of Dahua nephrite has eased the increasingly tight nephrite supply situation in China. Owing to its large reserves, the deposit has vast potential for future development. This material is of high quality and comes in a diverse array of colors including white, gray, light green, dark green, light yellow, and black. All bodycolors have been found to contain distinctive dendritic inclusions (figure 7). Dahua nephrite is popular with consumers, thus bringing huge economic benefit to the locality.

Dahua nephrite is mainly distributed around the river near the Yantan hydropower station. The ore body occurs in the limestone formed at the Qixian stage of the Paleozoic Permian system. The magmatic rocks in the area are basic intrusive rocks, divided into diabase and gabbro. The ore bed containing the nephrite is composed of dark gray stratified limestone of low to medium thickness, interspersed with fine calcite veins (B. Wang et al., "Gemmological and mineralogical characteristics of nephrite from Guangxi," *Journal of Gems and Gemmology*, Vol. 14, No. 3, 2012, pp. 6–11). The samples were tested by standard gemological methods, polarizing microscopy, environmental scanning electron microscopy (ESEM), X-ray diffraction (XRD), Raman spectroscopy, laser ablation–inductively

Figure 7. The nephrite samples with dendritic inclusions from Dahua County. Photos by Zuowei Yin.

coupled plasma–mass spectrometry (LA-ICP-MS), and energy-dispersive spectroscopy (EDS). We conducted the tests at the National Key Lab of the China University of Geosciences in Wuhan.

The refractive index of Dahua nephrites ranged from 1.60 to 1.63. The average hydrostatic specific gravity was 2.99, and the Mohs hardness was about 6.5. These properties were very similar to those of the samples previously tested, which had a spot RI of 1.61–1.62 and a hydrostatic SG of 2.88–2.90 (Yin et al., 2014).

The Raman spectra (peaks at 225, 370, 676, 1029, and 3677 cm^{-1}), infrared spectra, and X-ray powder diffraction (characteristic lines at 3.1189, 8.3968, 3.2702, and 2.7007 Å) were consistent with tremolite, showing that the main composition mineral of Dahua nephrite is tremolite with good crystallinity. Chemical composition analysis showed that the $Mg^{2+}/(Mg^{2+} + Fe^{2+})$ value of nephrite samples from Dahua was 0.973, identifying the main mineral as tremolite.

The REE distribution pattern of Dahua nephrite had an average value of Σ REE and LREE/HREE of 5.32 and 2.60, respectively, indicating that Dahua nephrite is slightly enriched in light rare earth elements. The δCe of the samples ranged from 0.21 to 0.91, with an average value of 0.47, in-

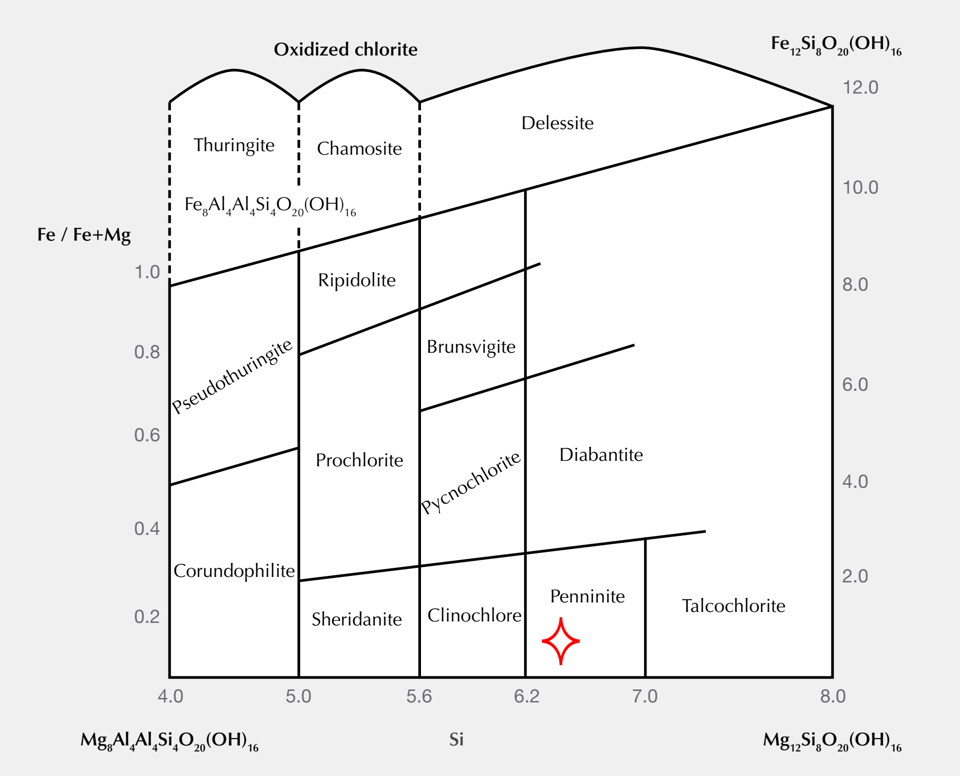

Figure 8. EDS compositional analysis showed that the chlorite inclusion in Dahua nephrite was penninite. From the chlorite classification system in Hu et al. (2019).

dicating a negative Ce anomaly. This suggests that Dahua nephrite was formed in a sedimentary metamorphic environment, with high oxygen fugacity and a single source of nephrite ore-forming fluid. The average δEu value of the samples was 0.71 in the range of 0.12–2.01, indicating a negative Eu anomaly. The negative Eu anomaly in this area may be due to the separation and crystallization during the ore-forming process of nephrite.

Most nephrite in Dahua has dendritic inclusions whose colors are mainly brownish yellow, brownish green, and black distributed in the form of branches, clumps, and the like. These "variegated" inclusions were actually determined to be penninite (belongs to the chlorite group) using modern techniques including routine gemstone testing, X-ray powder diffraction, scanning electron microscope, and EDS. According to the composition determined by EDS testing, we calculated the atomicity of Si with O_{20} as a reference. The results were as follows: The number of Si atoms was 6.4, and $Fe^{2+}/Fe + Mg$ was 0.16, indicating that the chlorite inclusion was a type of penninite (red cross in figure 8, from the chlorite classification scheme in Y. Hu et al., "Related studies on characteristic altered mineral chlorite," *West-China Exploration Engineering*, No. 11, 2019, pp. 132–134).

The variegated chlorite inclusions in Dahua nephrite are very useful identifying characteristics. With the exception of Luodian nephrite, which contains similar inclusions, such distinctive dendritic inclusions have yet to be discovered in white nephrite deposits; therefore, it is potentially a significant tracer for origin. The Dahua nephrite contains penninite, a type of chlorite (i.e., hydrothermally metamorphosed tremolite) (Yin et al., 2014). As an inclusion unique to Dahua nephrite, penninite serves as an important reference for origin tracing.

Zuowei Yin (yinzuowei1025@163.com), Wenwei Wang,
and Quanli Chen
Gemological Institute, China University of Geosciences
Wuhan, China

SYNTHETICS AND SIMULANTS

Spectral analysis of resin imitation ivory. The application of spectroscopic techniques in solving gemological challenges is becoming more routine since more data is needed than standard gemological testing can provide. For example, resin is composed of a variety of complicated chemical components and, while basic testing can identify whether the material is resin, further detailed examination must be undertaken to obtain the specific chemical composition.

A client submitted three "ivory" items for identification, a bead bracelet and two seal stamps (figure 9). This case is similar to the "resin imitation ivory with a pseudo 'engine-turned' structure" reported previously (Fall 2019 Lab Notes, pp. 419–421). Standard gemological testing revealed an RI of 1.54 (spot) and an SG of 1.23, with parallel linear striations, all very similar to the properties obtained from the samples in the case referenced above. Natural ivory normally indicates an RI of 1.54 (spot) and an SG of 1.85, with Schreger lines. By comparing with this case, further examinations were taken by the following procedures.

FTIR and Raman spectroscopy were used to analyze the differences between resin imitating ivory and natural ivory reference samples with a known provenance. These results were compared with those of the client's submissions.

As shown in figure 10 (top), mid-FTIR reflectance spectra from the natural ivory of known provenance revealed peaks at 1044, 1447, and 1559 cm^{-1} (related to biogenic hydroxyapatites); 1658, 2850, and 2919 cm^{-1} (consistent with collagen); and 3310 cm^{-1} (from CO_3^{2-}) (Z. Yin et al., "A comparison of modern and fossil ivories using multiple techniques," Spring 2013 *G&G*, pp. 16–27). The client's resin imitations revealed peaks at 702, 1126, 1284, 1380, 1462, and 1730 cm^{-1}, characteristic of ester group alkyd resins (figure 10, bottom) (S.M. Cakić et al., "Investigation of the curing kinetics of alkyd-melamine-epoxy resin system," *Progress in Organic Coatings*, Vol. 73, No. 4, 2012, pp. 415–424), and 2932 cm^{-1}, consistent with CH stretch-

Figure 9. The "ivory" items submitted for identification: a bracelet (left) consisting of 16 beads, 13.4 mm diameter each, and two seal stamps (right) measuring 20 × 80 mm each. Photos by Lai Tai-An Gem Lab.

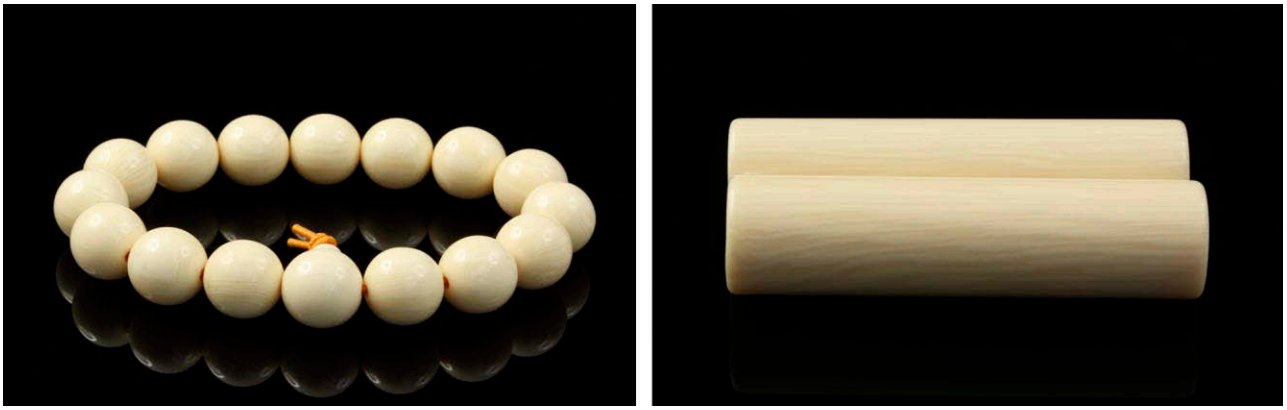

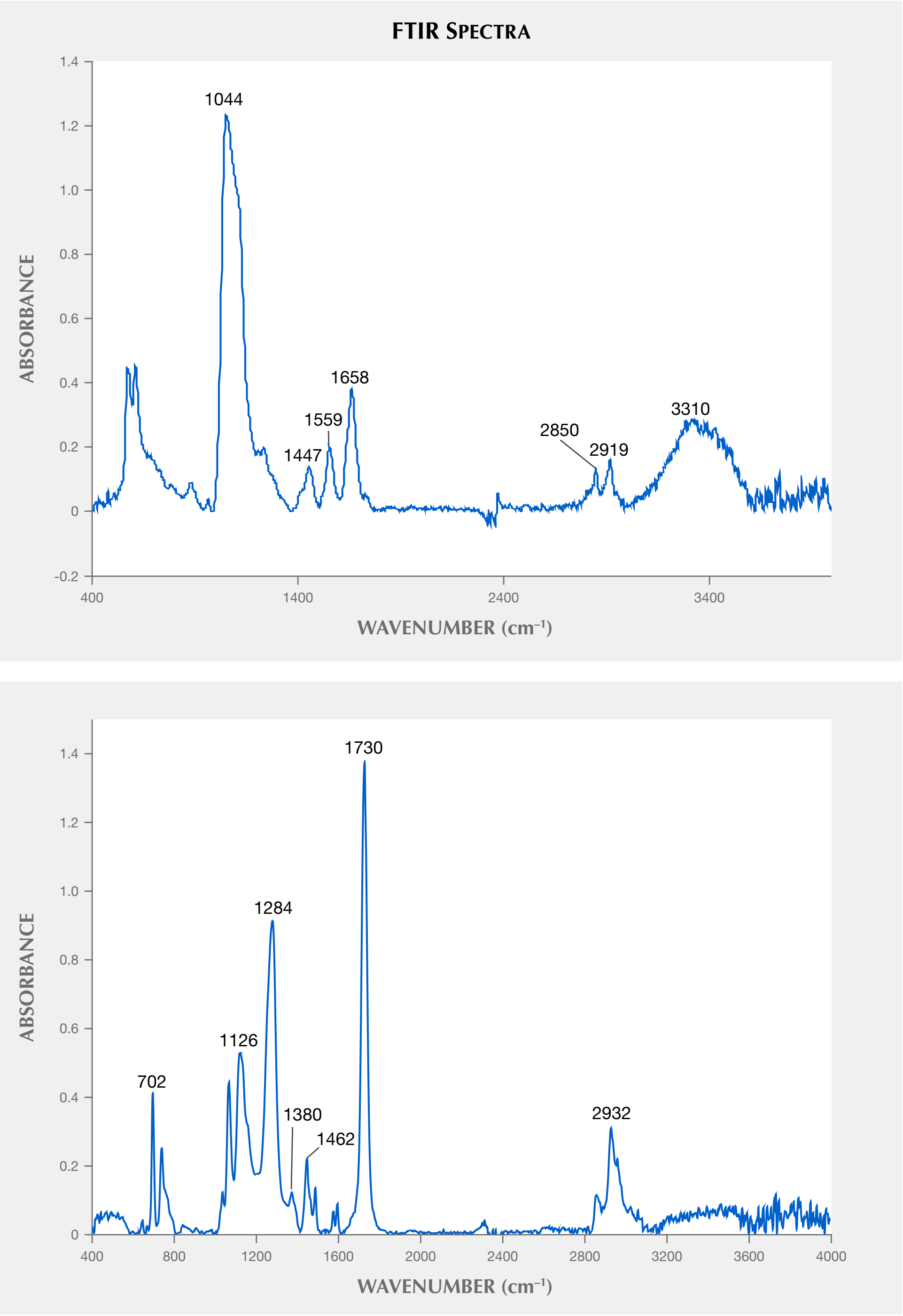

Figure 10. FTIR spectra of natural ivory (top) and this object "resin imitation ivory" (bottom) revealed different peaks.

ing. These results were significantly different from those obtained from known samples of ivory, as detailed above.

Raman analysis of the natural ivory revealed peaks at 428, 586, 852, 961, 1244, and 1664 cm^{-1} (figure 11, top), whereas the submitted resin samples displayed peaks at 621, 650, 1001, 1038, 1162, 1186, 1449, 1599, and 1724 cm^{-1} (figure 11, bottom). The spectra from each were sufficiently different to allow a quick and accurate separation.

These spectral comparisons provide readers with a reference when separating ivory from some resins. However, it is still important to apply standard gemological testing techniques during the initial examination while staying alert to the continual developments likely taking place with resin imitations. Spectral analysis plays an essential role in the differentiation process, especially in cases where more care may be needed.

Larry Tai-An Lai (service@laitaian.com.tw)
Lai Tai-An Gem Laboratory, Taipei

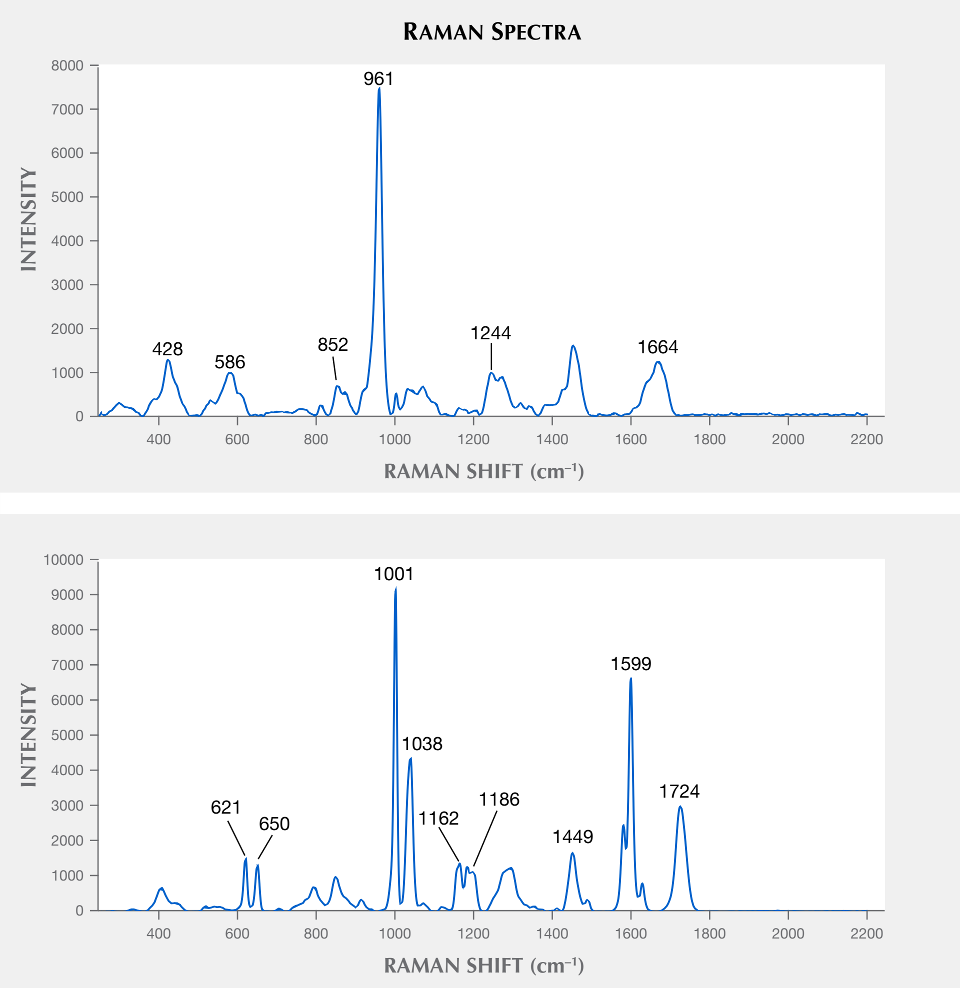

Figure 11. Raman spectra comparing natural ivory (top) and "resin imitation ivory" (bottom) also revealed significant differences.

A new phantom quartz imitation: Laser-engraved rock crystal. Phantom quartz generally refers to a rock crystal with inclusions of prismatic or pyramidal growth zonation, which represents early crystal faces covered by minerals, such as clinochlore, clay minerals, limonite, or fuchsite. Recently, a new type of phantom quartz imitation has appeared in the market, most of which is sold in the form of beads, pendants, or crystal spheres. A package of these imitation phantom quartz products was sent to the Taiwan Union Lab of Gem Research (TULAB) for identification services (figure 12).

These samples submitted as phantom quartz had a powdery white growth zonation in the form of a hexagonal pyramid. The host crystal was confirmed to be natural quartz by infrared absorption spectroscopy. The samples had an abnormal appearance for phantom quartz, of which the internal growth zonation was composed of regular and oriented small cracks (figure 13). Similar inclusions are often found in crafts made of glass or synthetic quartz engraved with a laser. According to the client, one of these

Figure 12. The "phantom quartz" pendant was later confirmed to be natural quartz with three-dimensional laser engraving. Photo by Shu-Hong Lin.

Figure 13. The internal growth zonation was composed of a regular network of small crack clusters around a central black point, presumably due to laser impact. Photomicrograph by Yu-Ho Li; field of view 2.14 mm.

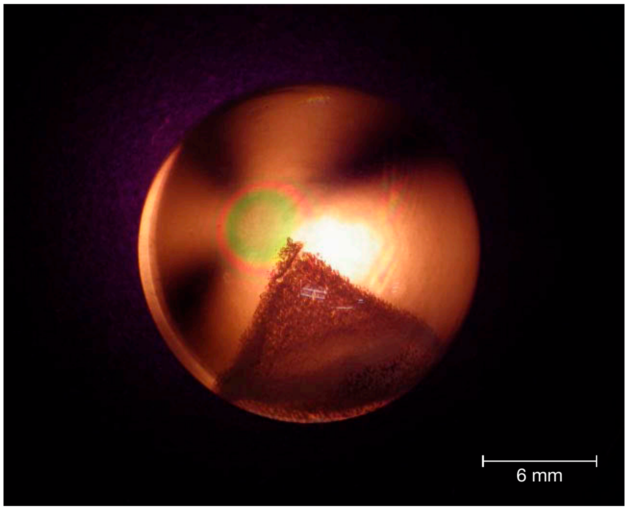

Figure 15. Crossed polarizers revealed that the bull's eye, indicating the optic axis, was nearly perpendicular to the axis of the engraved "phantom." Photo by Shu-Hong Lin.

samples had fractures along the ridgeline of the apparent pseudo-hexagonal pyramid (figure 14), which were possibly self- propagated due to the internal stress from the oriented small cracks.

In a true phantom, the axial direction of the host crystal is identical to that of the phantom crystal inside; however, the interference images through a polariscope revealed that the c-axis direction of these phantom quartz products was mostly inconsistent with what appeared to be their internal growth zonation (figure 15). In consideration of the morphological characteristics of inclusions as well as the interference images, these phantoms are imitations made of natural "rock crystal" with artificial growth zonation produced by laser engraving, irrespective of the crystallographic orientation of the host crystal.

Although internal laser engraving can imitate the appearance of a phantom quartz inclusion, such products can be easily identified through a microscope and a polariscope. More controversially, the internal stress generated by the regular and oriented cracks seems to reduce the toughness of the host crystal; therefore, consumers should be aware of the risk of such imitations.

Shu-Hong Lin
Institute of Earth Sciences, National Taiwan Ocean University
Taiwan Union Lab of Gem Research, Taipei

Yu-Ho Li
Institute of Earth Sciences, National Taiwan Ocean University

Huei-Fen Chen
Institute of Earth Sciences and Center of Excellence for Oceans
National Taiwan Ocean University

Figure 14. Left to right: A schematic diagram, a bottom view, and a top view of an imitation phantom crystal. The six fractures (red dashed lines) along the ridgeline of the pseudo-hexagonal pyramid in this imitation phantom quartz sphere were reportedly formed without any external force or heat treatment. The diameter of this sphere is 17.68 mm. Photos by Shu-Hong Lin.

TREATMENTS

Rhodium-plated iron meteorites. The annual Tucson Gem and Mineral Show has been a reliable source for the niche and the unusual, as seen with the rhodium-plated iron meteorites (figure 16) acquired by author BL at the 22nd Street Show in February 2020. The 28.53 ct mounted pendant and 36.69 ct loose slab were initially suspected to be imitations due to the abnormally high metallic luster and bright white color compared to typical polished and etched iron meteorites. However, chemical analysis of elements in the mounted sample using laser ablation–inductively coupled plasma–mass spectrometry (LA-ICP-MS) identified the specimens as authentic etched iron meteorites with layers of plated metals including nickel, copper, and rhodium.

Meteorites can be classified into three broad categories: stone, iron, and stony iron. The latter two groups are utilized within the gem and jewelry industry. The iron group consists of metallic meteorites composed primarily of iron with varying nickel content, a mineral intergrowth of low-nickel kamacite and high-nickel taenite. The iron group can be further categorized as hexahedrites (containing less than 6% nickel), octahedrites (6–13% nickel), and ataxites (more than 13% nickel) (O.R. Norton, *The Cambridge Encyclopedia of Meteorites*, 2002, pp. 184–198). When cut, polished, and etched with nital (a mixture of nitric acid and ethanol), the acid dissolves the isometric kamacite and taenite crystals at different rates, revealing a unique pattern dependent on the crystal's grain size. Octahedrites reveal a coarse pattern with a range of crystal widths known as a Widmanstätten structure (again, see figure 16). These lines and structures act like a fingerprint, as no two etched meteorites reveal the exact same pattern. Etched iron meteorites can also be easily classified by the size of their kamacite bands. Octahedrites show a width of banding ranging from 50 mm to < 0.2 mm. The pendant and slab showed an average band width of 0.50 mm and 2.68 mm, respectively, both well within the octahedrite threshold.

The pendant sample was analyzed with LA-ICP-MS spectrometry, and results were plotted and compared to a confirmed natural, non-plated octahedrite meteorite (figure 17). The x-axis shows time lapsed as the laser began drilling from the surface (starting at 40 seconds), therefore also representing depth. The y-axis shows the weight percent of the elements present. These include iron (Fe), nickel (Ni), copper (Cu), and rhodium (Rh) and represent the multiple layers of plating. The non-plated meteorite showed a steady amount of Fe (approximately 93 wt.%) and Ni (approximately 6 wt.%) throughout the total elapsed time from the beginning of analysis. The plated meteorite showed an initial thin peak of rhodium, quickly followed by a slightly wider peak of nickel. As these peaks began to flatten, a broad band of copper became visible. Near the 96 second mark, the graph of the plated meteorite began to resemble the non-plated meteorite, with approximately 92 wt.% Fe and 8 wt.% Ni. This analysis proved the material to be a genuine octahedrite meteorite with platings of Cu, Ni, and Rh. In order to achieve a final surface plating of rhodium to a metal, various under-platings are usually required. Through this technique of measuring the chemistry of the plated layers by LA-ICP-MS, gemologists were able to determine the identity of the subsurface material, as well as the composition of the various platings through a minimally destructive process. The pits or craters created by the laser are generally small (50 μm in diameter) and therefore impossible to visibly detect without magnification (L.A. Groat et al., "A review

Figure 16. The meteorite pendant (left) measured 27.02 × 12.75 × 2.59 mm and weighed 28.53 ct. The meteorite slab (right) measured 27.67 × 28.06 × 1.71 mm and weighed 36.69 ct. The intricate banding seen in these plated meteorites would both be categorized as Widmanstätten patterns, features of octahedrite iron meteorites. Photo by Angelica Sanchez.

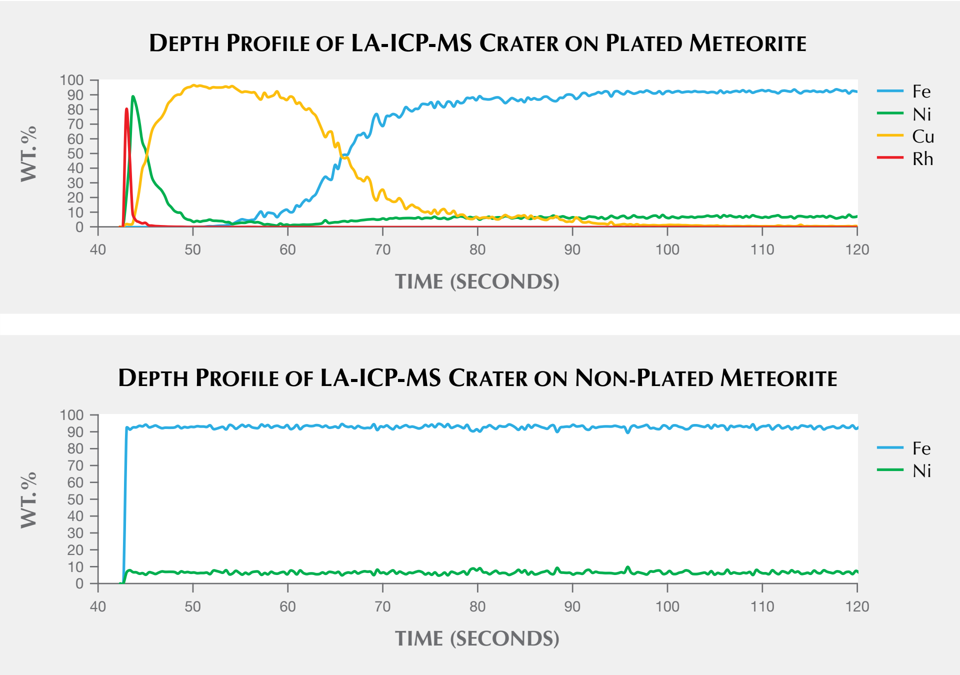

Figure 17. The profile of the plated meteorite (top) shows initial peaks of rhodium and nickel followed by a broad band of copper. Near the 96-second mark, the graph begins to resemble the profile of the non-plated meteorite (bottom) with >90 wt.% Fe and <10 wt.% Ni. This proves the material to be a genuine octahedrite meteorite with platings of Cu, Ni, and Rh.

of analytical methods used in geographic origin determination of gemstones," Winter 2019 *G&G*, pp. 512–535). Utilizing LA-ICP-MS to analyze metallic platings and subsurface materials is a method not previously explored by the authors. This study could offer insight into using LA-ICP-MS technology in new ways in the gem and jewelry industry.

Iron meteorites are prone to rusting due to their high iron content, as even slight humidity within air causes rapid corrosion. To slow this process, the stones are commonly kept in humidity-controlled environments, moisture absorbent silica gel, or coated with oil or hard clear lacquer. Rhodium plating offers an attractive luster and color to the surface; however, its essential function in this instance is to prevent moisture from altering the iron. Unfortunately, rust spots can be seen on the edges of both samples where the plating failed to adhere. Rhodium is a member of the platinum metal group, which is characterized by high stability, good resistance to corrosion, and a high melting point. While it is too brittle to be used for solid jewelry, rhodium has become a popular plating material, as it has a brighter color than silver or platinum.

Meteorites are popular collectibles with wide usage as jewelry. Etched iron meteorites can be found as watch dials and bezels, beads, hololith rings, and pendants. As this specialized material becomes more common, consumers should be aware of potential imitations or treatments such as these rhodium-plated examples.

Britni LeCroy, Ziyin Sun, and Dylan Hand
GIA, Carlsbad

Oiled tanzanite. Over the past five years, gemologists at Bangkok's Lotus Gemology have seen increasing numbers of what we might call "non-traditionally" oiled gems. This is particularly true of, but not limited to, Burmese gems such as ruby, sapphire, and spinel. But it is important to note that any gem with surface-reaching fissures can be oiled, often with dramatic improvements in apparent clarity. Cuprian and rubellite tourmalines are also frequently enhanced in this way.

Figure 18. This large 115 ct tanzanite was found to contain oil (left). After removal of the oil (center and right), highly reflective fissures became obvious. This clearly demonstrates how oiling a gem can have a radical impact on its appearance. Photos by Chanon Yimkeativong.

GIA

FRESHWATER PEARLS FROM A LABORATORY PERSPECTIVE

Global Pearl Development Conference (世界珍珠大会)
Nicholas Sturman, Consultant to GIA
13 November, 2020

Figure 19. GIA consultant Nicholas Sturman presented on freshwater pearls during the conference. Photo by Lin Chen.

Recently we received a faceted tanzanite weighing more than 100 carats for testing. As is our practice for non-emeralds exhibiting fissure-filling clarity enhancement, we photograph the gem and then allow the client to resubmit the stone after filler removal. Figure 18 clearly shows the dramatic effect that fissure filling with oil/resin can have on gems such as tanzanite, even where the refractive index of the filler does not closely match that of the gem.

Richard Hughes
Lotus Gemology, Bangkok

CONFERENCE REPORT

2020 World Pearl Congress. The World Pearl Congress was held November 13–15, 2020, in Shanxiahu Town, a division of the Chinese city of Zhuji. Known as "China's pearl capital," Shanxiahu Town is known for cultivating, processing, trading, and researching pearls, especially freshwater pearls. The town produces nearly 80% of China's pearls and is currently home to more than 2,500 pearl companies. This event was organized by CIBJO, the Gems and Jewelry Trade Association of China, the Zhejiang Provincial Committee of China Council for the Promotion of International Trade, and the Shaoxing Municipal People's Government.

The event consisted of a series of activities, presentations, and exhibitions focused on pearls. Despite the global pandemic, more than 400 attendees who live in China and represent a number of professions and industries attended this meeting in person, while several international and domestic speakers delivered a series of talks via prerecorded videos. Presentations included: "Freshwater Pearls from a Laboratory Perspective" (**Nicholas Sturman**, GIA consultant) (figure 19), "An Overview of the

Figure 20. The new World Freshwater Pearl Museum was recently opened in Zhuji, China. Photos by Lin Chen.

Global Pearl Industry" (**Kenneth Scarratt**, CIBJO Pearl Commission president), "Development of Quality and Detection of Pearls" (**Taijin Lu**, NGTC chief scientist), "The Importance of Design to the Pearl Industry" (**Paloma Sanchez**, independent designer), among many others. In addition, the World Freshwater Pearl Museum was also unveiled (figure 20), with exhibitions detailing the rich history of pearl culturing in China, pearl cultivating and processing techniques, and varieties of freshwater pearls and pearl jewelry.

According to several sources at the meeting, the global pandemic caused little disruption to the production of freshwater cultured pearls, as the harvest usually takes place at the end of the year and the government's fast control of the virus minimized the impact. However, the export of freshwater cultured pearls has been significantly affected, and dealers are trying to boost domestic sales with more emphasis on a strong online presence. Among different sales methods, livestreaming has become an ever more popular way to sell pearl jewelry in China (figure 21). From January to November 2020, online sales of pearls in Zhuji were valued at 11.85 billion yuan (US$1.8 billion), a year-over-year increase of 18.5%, according to Sina Finance.

Chunhui Zhou and Lin Chen
GIA, New York

ANNOUNCEMENT

American Gem Society upcoming events. The American Gem Society (AGS) will hold virtual and in-person educational events at the newly announced Confluence, slated for April 26. This event aims to provide industry professionals with content specifically designed to increase sales and refocus business strategy. Katherine Bodoh, CEO of AGS and AGS Laboratories, is pleased to offer a selection of programs that speak to "vital subjects our members need to reach new heights in their professional development." Members will also have access to AGS PRO, a learning portal filled with an array of relevant topics from leading experts in the field.

Conclave, which normally takes place each April, has been rescheduled for September 12–14, 2021. It will be held at the Sheraton Dallas Hotel in Dallas, Texas.

ERRATUM

The print version of the Spring 2020 article by Emily Dubinsky et al. ("A Quantitative Description of the Causes of Color in Corundum," pp. 2–28) contained several incorrectly colored gemstones and areal color density circles for various chromophores. To display the correct colors, we have included a reprint of the Spring 2020 article with this issue, accompanied by a wall chart.

Figure 21. Livestreaming has become one of the most popular ways for online selling of pearls in China, as shown in this Ruans store in Zhuji. Photo by Lin Chen.